ARTICLE

Corrected: Publisher Correction

https://doi.org/10.1038/s41586-018-0368-8

Functional aspects of meningeal lymphatics in ageing and Alzheimer's disease

Sandro Da Mesquita[1,2,10]*, Antoine Louveau[1,2,10], Andrea Vaccari[3,4], Igor Smirnov[1,2], R. Chase Cornelison[4], Kathryn M. Kingsmore[4], Christian Contarino[1,2,5], Suna Onengut-Gumuscu[6], Emily Farber[6], Daniel Raper[1,2,7], Kenneth E. Viar[1,2], Romie D. Powell[1,2], Wendy Baker[1,2], Nisha Dabhi[1,2], Robin Bai[1,2], Rui Cao[4], Song Hu[4], Stephen S. Rich[6], Jennifer M. Munson[4,8], M. Beatriz Lopes[9], Christopher C. Overall[1,2], Scott T. Acton[3,4] & Jonathan Kipnis[1,2]*

Ageing is a major risk factor for many neurological pathologies, but its mechanisms remain unclear. Unlike other tissues, the parenchyma of the central nervous system (CNS) lacks lymphatic vasculature and waste products are removed partly through a paravascular route. (Re)discovery and characterization of meningeal lymphatic vessels has prompted an assessment of their role in waste clearance from the CNS. Here we show that meningeal lymphatic vessels drain macromolecules from the CNS (cerebrospinal and interstitial fluids) into the cervical lymph nodes in mice. Impairment of meningeal lymphatic function slows paravascular influx of macromolecules into the brain and efflux of macromolecules from the interstitial fluid, and induces cognitive impairment in mice. Treatment of aged mice with vascular endothelial growth factor C enhances meningeal lymphatic drainage of macromolecules from the cerebrospinal fluid, improving brain perfusion and learning and memory performance. Disruption of meningeal lymphatic vessels in transgenic mouse models of Alzheimer's disease promotes amyloid-β deposition in the meninges, which resembles human meningeal pathology, and aggravates parenchymal amyloid-β accumulation. Meningeal lymphatic dysfunction may be an aggravating factor in Alzheimer's disease pathology and in age-associated cognitive decline. Thus, augmentation of meningeal lymphatic function might be a promising therapeutic target for preventing or delaying age-associated neurological diseases.

For decades, the CNS has been seen as an immune privileged organ[1], because of its limited interactions with the immune system, especially under homeostatic, healthy conditions[2,3]. Immune cells do not enter the parenchyma of the healthy brain as such; the surveillance of the CNS takes place within the meningeal spaces, where a great variety of immune cells is found[2,3]. Our group, along with others[4,5], has recently (re)discovered and characterized the lymphatic vessels within the meninges (of rodents[4], non-human primates and humans[6]), although the role of these vessels in CNS function and in pathologies remains unclear.

Body tissues are perfused by interstitial fluid (ISF), which is locally reabsorbed via the lymphatic vascular network. By contrast, the parenchyma of the CNS is devoid of lymphatic vasculature[2]; in the brain, removal of cellular debris and toxic molecules, such as amyloid-β peptides, is mediated by a combination of transcellular transport mechanisms across the blood–brain and blood–cerebrospinal fluid (CSF) barriers[7–9], phagocytosis and digestion by resident microglia and recruited monocytes and/or macrophages[10,11], as well as CSF influx and ISF efflux through a paravascular (glymphatic) route[12–14]. The (re) discovery and characterization of meningeal lymphatic vessels has led to a reassessment of the pathways for the clearance of waste from the CNS[4,5]. The role of this vasculature in brain function, specifically in the context of ageing and Alzheimer's disease, has not been studied. Alzheimer's disease is the most common form of dementia and its prevalence increases with age[15,16]. Extracellular deposition of amyloid-β aggregates, the main constituent of senile plaques, is considered to be a pathological hallmark of Alzheimer's disease that contributes to neuronal dysfunction and behavioural changes[16,17]. It is interesting to note that the amyloid-β protein was initially isolated from homogenates of meningeal tissue from patients with Alzheimer's disease[18]. However, the mechanisms that underlie the accumulation of amyloid-β in the brain and meninges of patients with Alzheimer's disease are still not fully understood. The ageing-associated decrease in paravascular recirculation of CSF and ISF[13] is thought to be responsible, at least in part, for the accumulation of amyloid-β in the brain parenchyma[12,13,19]. Ageing also leads to progressive lymphatic vessel dysfunction in peripheral tissues[20–22]. However, little is known about a possible functional decay of the CSF-draining meningeal lymphatic vessels with age and how this decay might influence CNS amyloid-β pathology in Alzheimer's disease.

Here we show that meningeal lymphatic vessels have an essential role in maintaining brain homeostasis by draining macromolecules from the CNS (both CSF and ISF) into the cervical lymph nodes. Using pharmacological, surgical and genetic models, we show that impairment or enhancement of meningeal lymphatic function in mice affects paravascular influx of CSF macromolecules, efflux of ISF macromolecules and cognitive task performance. Our findings demonstrate that meningeal lymphatic vessel dysfunction may be one of the underlying factors for worsened amyloid-β pathology and cognitive deficits in Alzheimer's disease and might be therapeutically targeted to alleviate age-associated cognitive decline.

Meningeal lymphatics and brain perfusion

Given the close communication and continuous exchange of molecular contents between the CSF and ISF[5,12], we hypothesized that brain influx of CSF macromolecules through the paravascular pathway is affected by the meningeal lymphatic vessels. To test this hypothesis, we

[1]Center for Brain Immunology and Glia (BIG), University of Virginia, Charlottesville, VA, USA. [2]Department of Neuroscience, University of Virginia, Charlottesville, VA, USA. [3]Virginia Image and Video Analysis Laboratory, Department of Electrical and Computer Engineering, University of Virginia, Charlottesville, VA, USA. [4]Department of Biomedical Engineering, University of Virginia, Charlottesville, VA, USA. [5]Department of Mathematics, University of Trento, Povo, Italy. [6]Center for Public Health Genomics, University of Virginia, Charlottesville, VA, USA. [7]Department of Neurosurgery, University of Virginia Health System, Charlottesville, VA, USA. [8]Department of Biomedical Engineering and Mechanics, College of Engineering, Virginia Tech, Blacksburg, VA, USA. [9]Department of Pathology, University of Virginia, Charlottesville, VA, USA. [10]These authors contributed equally: Sandro Da Mesquita, Antoine Louveau. *e-mail: sd8tf@virginia.edu; kipnis@virginia.edu

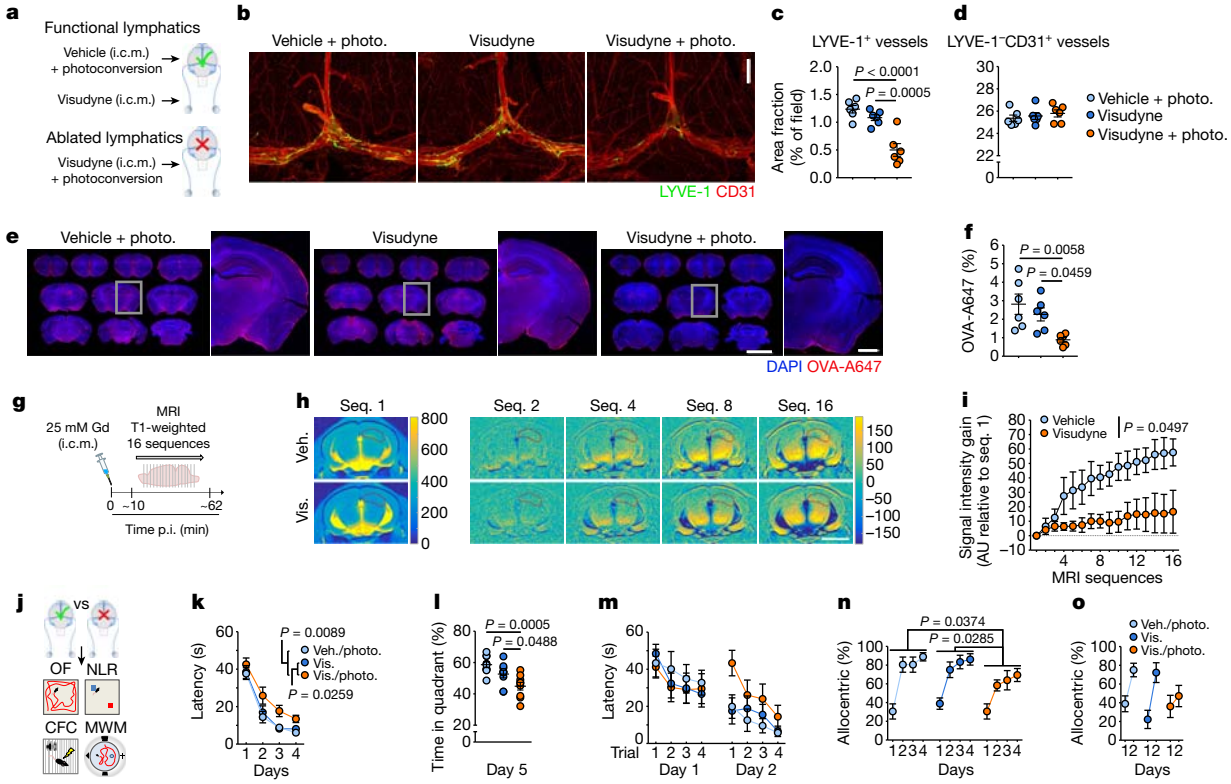

Fig. 1 | Impairing meningeal lymphatics affects brain CSF influx and ISF diffusion and worsens cognitive function. a, Seven days after lymphatic ablation, mice were injected with 5 μl of OVA-A647 i.c.m. **b**, Representative images of meningeal whole-mounts stained for LYVE-1 and CD31. Scale bar, 1 mm. **c**, **d**, Quantification of area fraction (%) occupied by LYVE-1$^+$ lymphatic vessels (**c**) and LYVE-1$^-$CD31$^+$ blood vessels (**d**). **e**, Representative brain sections showing 4′,6-diamidino-2-phenylindole (DAPI) and OVA-A647. Scale bars, 5 mm and 1 mm (inset). **f**, Quantification of OVA-A647 area fraction. Data in **c**, **d** and **f** are mean ± s.e.m., $n = 6$ per group, one-way ANOVA with Bonferroni's post hoc test. **a**–**f**, Data are representative of two independent experiments; significant differences between vehicle (Veh.) with photoconversion (photo.) and visudyne (Vis.) with photoconversion were replicated in five independent experiments. **g**, Gd was injected (i.c.m.) and T1-weighted MRI acquisition was performed seven days after meningeal lymphatic ablation. p.i., post injection. **h**, Representative images of sequence (Seq.) 1 and of Gd intensity gain in subsequent sequences. The hippocampus is delineated in red. Scale bar, 3 mm. **i**, Quantification of the Gd signal intensity gain over 16 sequences (relative to sequence 1) in hippocampus. Data in **i** are mean ± s.e.m., $n = 4$ per group, repeated-measures two-way ANOVA with Bonferroni's post hoc test. **g**–**i** Data are representative of two independent experiments. **j**, Meningeal lymphatic ablation was performed twice and two weeks after the last intervention, open field (OF), NLR, CFC and MWM behavioural tests were performed (see Extended Data Fig. 5 for open field, NLR and CFC tests). **k**, Latency to platform (acquisition). **l**, Percentage of time spent in the target quadrant (probe). **m**, Latency to platform (reversal). **n**, **o**, Allocentric navigation strategies (%) used in the MWM acquisition (**n**) and reversal (**o**). Data in **k**–**o** are mean ± s.e.m., $n = 9$ per group; repeated-measures two-way ANOVA with Bonferroni's post hoc test (**k**, **m**–**o**), one-way ANOVA with Bonferroni's post hoc test (**l**); significant differences between vehicle with photoconversion and visudyne with photoconversion were replicated in three independent experiments.

ablated meningeal lymphatic vessels by injecting a photodynamic drug, visudyne (also known as verteporfin for injection), into the CSF, which upon photoconversion has been shown to preferentially damage the lymphatic endothelial cells (LECs)[23,24]. Injections of vehicle followed by photoconversion and injections of visudyne without the photoconversion step were used as two controls (Fig. 1a). The use of this method resulted in effective ablation of meningeal lymphatic vessels (Fig. 1b, c), without any detectable off-target effects in the coverage of meningeal blood vasculature seven days after the procedure (Fig. 1d). To confirm functional impairment after meningeal lymphatic vessel ablation, we injected 5 μl of fluorescent ovalbumin–Alexa Fluor 647 (OVA-A647; approximately 45 kDa) into the cisterna magna (i.c.m.) and measured the drainage of this tracer from the CSF into the deep cervical lymph nodes (dCLNs) (Extended Data Fig. 1a). A significant reduction in OVA-A647 drainage was observed in the visudyne with photoconversion group compared to the control groups (Extended Data Fig. 1b). Notably, the structure of major intracranial veins and arteries was not altered (Extended Data Fig. 1c–h). Similarly, the integrity of the blood–brain barrier, assessed by T1-weighted magnetic resonance imaging (MRI) after intravenous injection of gadolinium (Gd) as contrast agent (Extended Data Fig. 1i, j), and the ventricular volume measured by T2-weighted SPACE (sampling perfection with application optimized contrasts using different flip angle evolution) MRI (Extended Data Fig. 1k–m) also remained unaltered after ablation of meningeal lymphatic vessels.

To avoid any confounding effects due to increased intracranial pressure (ICP) after i.c.m. injection, we measured changes in ICP after injecting different volumes of OVA-A647 (Extended Data Fig. 2a, b). There was a transient increase in ICP during i.c.m. injection of the tracer, followed by a drop in ICP upon removal of the syringe after the injection (Extended Data Fig. 2a). Mice injected with 2 μl presented ICP values lower than baseline even 120 min post-injection (Extended Data Fig. 2b). Notably, ablation of meningeal lymphatic vessels led to an equal decrease in drainage to the dCLNs in mice upon injection of 2 μl (Extended Data Fig. 2c–e) or 5 μl of the tracer (Extended Data Fig. 1a, b).

Brain perfusion by the CSF tracer was found to be significantly lower in the visudyne with photoconversion group than in the control groups (Fig. 1e, f and Extended Data Fig. 2f, g). Similar findings for brain perfusion by CSF were observed when meningeal lymphatic drainage was disrupted by surgical ligation of the vessels afferent to the dCLNs (Extended Data Fig. 3a–d). Prospero homeobox protein 1 heterozygous (*Prox1*$^{+/-}$) mice, a genetic model of lymphatic vessel malfunction[25], also presented impaired perfusion through the brain parenchyma and impaired CSF drainage (Extended Data Fig. 3e–i). Together, three

different models of impaired meningeal lymphatic function (pharmacological, surgical and genetic) showed a significant impact on brain perfusion by CSF macromolecules.

To evaluate the effect of meningeal lymphatic ablation on the rate of brain perfusion by CSF, we injected Gd (i.c.m.) and performed brain T1-weighted MRI. Three different concentrations of Gd—1, 10 and 25 mM—were tested (Extended Data Fig. 3j, k) and, owing to a better signal-to-noise ratio, the concentration of 25 mM was used in subsequent experiments (Fig. 1g). A software package developed in-house, Lymph4D (see Supplementary Methods for more details), was used to process and analyse the images acquired by MRI. After 16 sequences of MRI acquisition (around 52 min), the observed signal gain in two brain regions (hippocampus and cortex) was significantly lower in the visudyne group compared to vehicle group (Fig. 1h, i and Extended Data Fig. 3l, m). Notably, along with the lower influx of Gd into the parenchyma, we observed higher contrast in signal intensity (over approximately 52 min) in the ventricles of visudyne-treated mice, suggesting that Gd accumulation in the CSF occurred (Extended Data Fig. 3n). Whether this observation is concomitant with ventricular CSF reflux (a phenomenon reported in patients with idiopathic normal-pressure hydrocephalus[26]) warrants further investigation. Moreover, using the advection–diffusion model in Lymph4D, we found that mice had lower coefficient values of isotropic diffusion of Gd in the brain after meningeal lymphatic ablation (Extended Data Fig. 3o, p), suggesting that there is a lower rate of molecular diffusion in the brain parenchyma when meningeal lymphatic drainage is reduced.

Within the brain parenchyma, it was shown that aquaporin 4 (AQP4) expression by astrocytes plays an important role in the modulation of paravascular CSF macromolecule influx and efflux (through the glymphatic route)[12,13]. Deletion of *Aqp4* in transgenic mice with Alzheimer's disease also resulted in increased amyloid-β plaque burden and exacerbated cognitive impairment[19]. Moreover, decreased perivascular AQP4 localization was observed in brain tissue from patients with Alzheimer's disease[27]. We did not detect changes either in overall brain coverage by AQP4 (Extended Data Fig. 3q, r) or in perivascular localization of $AQP4^+$ astrocytic endfeet between vehicle-treated and visudyne-treated mice (Extended Data Fig. 3s–v), suggesting that upon meningeal lymphatic ablation, impairment of brain perfusion by CSF is independent of AQP4.

Next, we examined whether the efflux of ISF macromolecules from the brain parenchyma would also be affected by meningeal lymphatic vessels. We used three different tracers, the smaller peptides amyloid-β_{42}–HyLite647 (approximately 4 kDa) and OVA-A647, and the large protein complex, low-density lipoprotein–BODIPY FL (LDL–BODIPY FL, around 500 kDa). One hour after stereotaxic injection, the levels of the remaining tracers were assessed in the parenchyma of mice in which the lymphatic vessels were ablated and in mice from the control groups (Extended Data Fig. 4a–h). Independently of the nature of the fluorescent tracer, higher levels of remnants were detected in the brains of mice from the visudyne with photoconversion groups compared to both control groups (Extended Data Fig. 4a–h). These findings, as has been suggested previously[5], demonstrate that the efflux of parenchymal and/or ISF macromolecules and the drainage of these macromolecules into dCLNs are impaired as a consequence of meningeal lymphatic ablation, thus functionally connecting meningeal lymphatics with CSF influx and ISF efflux mechanisms.

To understand the implications of impaired meningeal lymphatic drainage for brain function, we performed meningeal lymphatic ablation twice, allowing a two-week interval between procedures to ensure prolonged lymphatic ablation, and then assessed the behaviour of mice in the open field, novel location recognition (NLR), contextual fear conditioning (CFC) and Morris water maze (MWM) tests (Fig. 1j). No differences between the groups were detected in total distance travelled and time spent in the centre of the arena in the open field test (Extended Data Fig. 5a, b) or in time spent with the object placed in a novel location in the NLR test (Extended Data Fig. 5c, d). A significant difference between control groups and visudyne with photoconversion group was observed in the cued test of the CFC (Extended Data Fig. 5e, f), which points to an impairment in fear memory and in hippocampal–amygdala neuronal circuitry[28] in mice with impaired meningeal lymphatic vessel function. Mice with ablated meningeal lymphatic vessels also showed significant deficits in spatial learning in the MWM (Fig. 1k–o). Similar impairments in spatial learning and memory were observed in mice that had undergone lymphatic ligation (Extended Data Fig. 5g–j), supporting the notion that the observed effect is a result of dysfunctional meningeal lymphatic drainage and not an artefact of the ablation method using visudyne.

Using RNA sequencing (RNA-seq), we assessed the effect of visudyne treatment with photoconversion on hippocampal gene expression before and after the MWM. Principal component analysis showed that four weeks of meningeal lymphatic ablation did not induce significant changes in the hippocampal transcriptome (Extended Data Fig. 5k, l). However, significant differences in hippocampal gene expression were found in response to MWM performance after prolonged meningeal lymphatic ablation (Extended Data Fig. 5m, n). Contrary to what was observed without MWM performance (Extended Data Fig. 5k, l), individual samples from each group clustered together after the mice performed the test (Extended Data Fig. 5m, n). Notably, although the fold change in significantly altered genes after lymphatic ablation and MWM was moderate ($-1.79 < \log_2(\text{fold change}) < 1.69$), functional enrichment analysis (Extended Data Fig. 5o, p) revealed changes in gene sets associated with neurodegenerative diseases, such as Huntington's, Parkinson's and Alzheimer's disease (Extended Data Fig. 5o). Significant transcriptional alterations were also associated with excitatory synaptic remodelling and plasticity, hippocampal neuronal transmission[29], learning and memory and ageing-related cognitive decline[30] (Extended Data Fig. 5q, r). Furthermore, different gene sets that are involved in the regulation of metabolite generation and processing, glycolysis and mitochondrial respiration and oxidative stress were also significantly altered in the hippocampus upon lymphatic ablation and performance of the behaviour test (Extended Data Fig. 5p, s–v).

Meningeal lymphatic vessels during ageing

Ageing is the principal risk factor for many neurological disorders, including Alzheimer's disease[15,16], and has a detrimental effect on CSF and ISF paravascular recirculation within the brain[13]. The reported findings that ageing is also associated with peripheral lymphatic dysfunction[20–22] led us to hypothesize that the deterioration of meningeal lymphatic vessels underlies some aspects of age-associated cognitive decline. Indeed, and in agreement with a previous study[13], old mice demonstrate reduced brain perfusion by CSF macromolecules compared to young counterparts (Extended Data Fig. 6a, b). Impaired brain perfusion by CSF in old mice was accompanied by a decrease in meningeal lymphatic vessel diameter and coverage, as well as decreased drainage of CSF macromolecules into dCLNs in both females and males (Extended Data Fig. 6c–f). To further address the effect of ageing on meningeal lymphatic vessels, we performed RNA-seq analysis of LECs sorted from the meninges of young-adult (2–3 months of age) and old (20–24 months of age) mice (Fig. 2a–d and Extended Data Fig. 6g). Differential expression of 607 genes was detected in the meningeal LECs of old compared to young–adult mice (Fig. 2a). Of note, the expression of genes that encode classical markers of LECs, including *Flt4*, which encodes the vascular endothelial growth factor C (VEGF-C) receptor tyrosine kinase VEGFR3, was not significantly altered at 20–24 months (Fig. 2b). Enrichment analysis revealed, however, changes in gene sets involved in immune and inflammatory responses, phospholipid metabolism, extracellular matrix organization, cellular adhesion and endothelial tube morphogenesis, all of which suggest that there are functional alterations in meningeal LECs with age (Fig. 2c). The altered expression of genes involved in the transmembrane receptor protein tyrosine kinase signalling pathway in old mice, namely the downregulation of *Cdk5r1*[31], *Adamts3*[32] and *Fgfr3*[33], indicated possible changes in signalling by lymphangiogenic growth factors in old meningeal LECs (Fig. 2d).

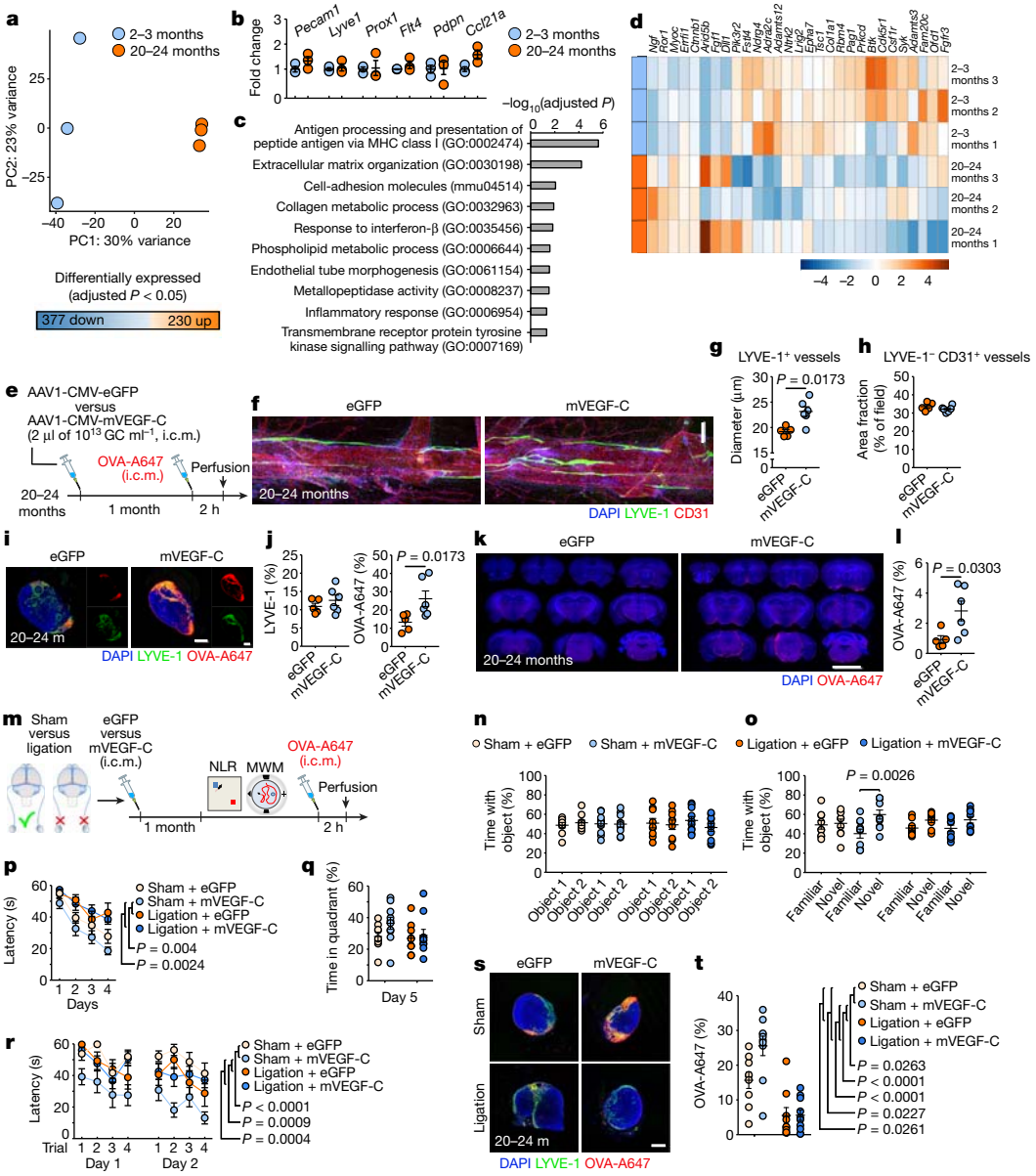

Fig. 2 | Improving meningeal lymphatic function in aged mice increases brain perfusion and alleviates cognitive deficits. a, Principal component (PC) analysis plot for RNA-seq of LECs from meninges of young–adult and aged mice. There were 230 genes up- and 377 genes downregulated in meningeal LECs at 20–24 months (m). **b**, Expression of *Pecam1*, *Lyve1*, *Prox1*, *Flt4*, *Pdpn* and *Ccl21a*. **c**, Gene sets obtained by functional enrichment of differentially expressed genes in meningeal LECs at 20–24 months. **d**, Heat map showing relative expression level of genes involved in the transmembrane receptor protein tyrosine kinase signalling pathway. Colour scale bar values represent standardized rlog-transformed values across samples. Data in **a**–**d** consist of $n = 3$ per group (individual RNA samples result from LECs pooled from 10 meninges over two independent experiments); data in **b** are mean ± s.e.m. with two-way ANOVA with Bonferroni's post hoc test; in **a**–**c** *P* values were corrected for multiple hypothesis testing with the Benjamini–Hochberg false-discovery rate procedure; in **c**, **d** functional enrichment of differential expressed genes was performed using gene sets from Gene Ontology (GO) and Kyoto Encyclopedia of Genes and Genomes (KEGG) and determined with Fisher's exact test. **e**, Old mice were injected (i.c.m.) with 2 µl of AAV1-CMV-eGFP (eGFP) or AAV1-CMV-mVEGF-C (mVEGF-C), at 10^{13} genome copies (GC) ml^{-1}. One month later, OVA-A647 was injected i.c.m. **f**, Insets of the superior sagittal sinus showing DAPI, LYVE-1 and CD31 staining. Scale bar, 200 µm. **g**, **h**, Quantification of the diameter of LYVE-1$^+$ lymphatic vessels (**g**) and the area fraction (%) of LYVE-1$^-$CD31$^+$ blood vessels (**h**). **i**, Representative sections of dCLNs showing DAPI, LYVE-1 and OVA-A647 staining. Scale bar, 200 µm. **j**, Quantification of LYVE-1 and OVA-A647 area fraction in dCLNs. **k**, Representative brain coronal sections showing DAPI and OVA-A647 staining. Scale bar, 5 mm. **l**, Quantification of OVA-A647 area fraction in brain sections. Data in **g**, **h**, **j**, **l** are mean ± s.e.m., $n = 5$ mice treated with eGFP, $n = 6$ mice treated with mVEGF-C, two-tailed Mann–Whitney *U*-test; **e**–**l**, Data are representative of two independent experiments. **m**, Old mice were injected with eGFP or mVEGF-C viruses (i.c.m.) after ligation of the lymphatic vessels afferent to the dCLNs or sham surgery. One month later, learning and memory was assessed in the NLR and MWM tests and mice were injected (i.c.m.) with OVA-A647. **n**, **o**, Time with the object (%) was assessed in the training (**n**) and novel location (**o**) tasks of the NLR test. **p**, Latency to platform (acquisition). **q**, Percentage of time spent in the target quadrant (probe). **r**, Latency to platform (reversal). **s**, Representative sections of dCLNs showing DAPI, LYVE-1 and OVA-A647 staining. Scale bar, 200 µm. **t**, Quantification of OVA-A647 area fraction in dCLNs. Data in **n**–**r**, **t** are mean ± s.e.m., $n = 9$ in sham with eGFP and ligation with eGFP groups, $n = 10$ in sham with mVEGF-C and ligation with mVEGF-C groups, two-way ANOVA with Bonferroni's post hoc test (**n**, **o**, **q**, **t**), repeated-measures two-way ANOVA with Bonferroni's post hoc test (**p**, **r**); **m**–**t** results from two independent experiments.

We have previously shown that treatment with recombinant VEGF-C increases the diameter of meningeal lymphatic vessels[4]. Furthermore, delivery of VEGF-C by adenoviral gene therapy was previously found to efficiently boost peripheral lymphatic sprouting and function[34,35]. A similar adeno-associated virus serotype 1 (AAV1) vector was used here to express mouse (m)VEGF-C or enhanced green fluorescent

protein (eGFP) as control. At two and four weeks post i.c.m. injection, AAV1-infected cells expressing eGFP were found to be limited to the pia around the brain, meninges (dura and arachnoid), and pineal gland (Extended Data Fig. 6h–j). Treatment of young mice with AAV1-CMV-mVEGF-C resulted in a significant increase in meningeal lymphatic vessel diameter, without affecting blood vessel coverage (Extended Data Fig. 6k–m).

Treatment of old mice (at 20–24 months) with AAV1-CMV-mVEGF-C also resulted in increased lymphatic vessel diameter (compared to AAV1-CMV-eGFP) without detectable off-target effects on the meningeal blood vasculature coverage and on meningeal and/or brain vascular haemodynamics (Fig. 2e–h and Extended Data Fig. 6n–p). One month after AAV1-CMV-mVEGF-C treatment, old mice showed a significant increase in CSF tracer drainage into the dCLNs, which was not due to increased lymphatic vessel coverage in the nodes (Fig. 2i, j). Notably, the rate of tracer influx into the brain parenchyma was significantly increased as a result of enhanced meningeal lymphatic function (Fig. 2k, l and Extended Data Fig. 6q, r).

Transcranial delivery (through a thinned skull surface) of hydrogel-encapsulated VEGF-C peptide also resulted in increased diameter of meningeal lymphatics in young and old mice (Extended Data Fig. 7a–c). This VEGF-C treatment led to a significant increase in the function of meningeal lymphatic vessels in old mice, whereas young–adult mice did not respond to the treatment (Extended Data Fig. 7d, e), probably due to the ceiling effect of their existing capacity to drain OVA-A647. The increased drainage after VEGF-C treatment in old mice also correlated with enhanced brain perfusion by CSF macromolecules (Extended Data Fig. 7f, g).

To avoid potential off-target effects of VEGF-C on the blood vasculature through VEGFR2, we carried out transcranial delivery of VEGF-C156S (Extended Data Fig. 7h), a mutated version of VEGF-C that binds specifically to VEGFR3 and spares its effects on VEGFR2[34,36]. Treatment with VEGF-C156S resulted in a significant increase in meningeal lymphatic diameter (Extended Data Fig. 7i, j), drainage of tracer from the CSF (Extended Data Fig. 7k, l), and paravascular influx of tracer into the brains of old mice (Extended Data Fig. 7m, n).

To determine the functional role of enhanced meningeal lymphatics in the learning behaviour of mice at different ages, we again used viral delivery of mVEGF-C (Extended Data Fig. 7o–u). This method was selected to avoid submitting aged mice to consecutive surgeries, involving general anaesthesia and skull thinning. Treatment of young–adult mice with AAV1-CMV-mVEGF-C for 1 month did not improve spatial learning and memory (Extended Data Fig. 7p, s), suggesting that there is a ceiling effect in MWM performance at this age. However, AAV1-CMV-mVEGF-C treatment resulted in significant improvement in the latency to platform and in the percentage of allocentric navigation strategies, in the MWM reversal at 12–14 months (Extended Data Fig. 7q, t) and in the MWM acquisition and reversal at 20–22 months (Extended Data Fig. 7r, u), compared to AAV1-CMV-eGFP-treated age-matched mice.

Increased expression of VEGF-C in the adult brain has previously been shown to boost proliferation of neural stem cells in the hippocampus[37]. Although spatial learning and memory in the MWM is not dependent on adult hippocampal neurogenesis[38], we examined the number of Ki-67-expressing cells in the hippocampal dentate gyrus of mice treated with eGFP or mVEGF-C viral vectors at 3, 12–14 and 20–22 months of age. No differences in cell proliferation in the dentate gyrus were observed after mVEGF-C treatment (Extended Data Fig. 7v, w).

To demonstrate that the beneficial effect of mVEGF-C treatment on cognitive behaviour was through improved drainage of meningeal lymphatic vessels, we injected old mice with the eGFP or mVEGF-C viruses and concomitantly ligated the lymphatic vessels afferent to dCLNs. Assessment of learning and memory was performed one month after the procedures (Fig. 2m). The beneficial effect of mVEGF-C treatment in mice from the sham group, which performed significantly better in the NLR (Fig. 2n, o) and MWM (Fig. 2p–r) tests, was abrogated in mice in which the CSF-draining lymphatic vessels had been ligated. Accordingly, the drainage of CSF macromolecules into dCLNs was significantly higher in sham-operated mice treated with mVEGF-C compared to all other groups (Fig. 2s, t).

Dysfunctional lymphatic vessels in amyloid-β pathology

On the basis of previous findings concerning the role of paravascular CSF and ISF recirculation in the context of Alzheimer's disease[12,14,19,27] and our present results on the interdependence between meningeal lymphatic function and brain perfusion by CSF, we proposed that modulating meningeal lymphatic function would impact the behaviour of and brain pathology in transgenic mice with Alzheimer's disease. The potential effect of mVEGF-C treatment (through viral vector delivery) was first tested on J20 transgenic mice at 6–7 months of age (Extended Data Fig. 8a–n), when mice already present marked cognitive deficits and start to show amyloid-β deposition in the brain parenchyma[39,40]. We were not able to improve the hyperactive phenotype of J20 mice in the open field or cognitive performance in the MWM (Extended Data Fig. 8a–f). Moreover, viral expression of mVEGF-C did not significantly affect the diameter of meningeal lymphatic vessels, the level of amyloid-β in the CSF, or amyloid-β deposition in the hippocampus (Extended Data Fig. 8g–n). In order to explain the lack of effect of the mVEGF-C treatment in J20 mice, we measured meningeal lymphatic drainage in J20 mice and in wild-type littermate controls. The same measurement was performed in a more aggressive transgenic mouse model of Alzheimer's disease, the 5xFAD mice, which already have amyloid-β plaques at three months of age[41] (Extended Data Fig. 8o). Independently of the model, the level of CSF tracer drained into the dCLNs was comparable between transgenic mice with Alzheimer's disease and age-matched wild-type littermates (Extended Data Fig. 8p–s). Similarly, the morphology and coverage of meningeal lymphatic vessels did not differ between wild-type and 5xFAD mice at 3–4 months of age (Extended Data Fig. 8t, u). Collectively, these data point to no apparent meningeal lymphatic dysfunction in transgenic mice with Alzheimer's disease at younger ages, which might explain the inefficacy of mVEGF-C treatment.

Although age is the major risk factor for late-onset Alzheimer's disease[15,16], most transgenic mouse models that mimic early-onset Alzheimer's disease develop amyloid-β pathology at young age and, therefore, may be lacking the aspect of age-related lymphatic dysfunction. To this end, we induced prolonged meningeal lymphatic ablation in 5xFAD mice by repeated (every three weeks) injection and photoconversion of visudyne for a total of 1.5 months, starting at around two months of age (Fig. 3a). Taking into account the marked deposition of amyloid-β in the brain that these mice have at approximately three months of age, surprisingly, no obvious amyloid-β deposition was detected in the meninges of 5xFAD mice from the two control groups (Fig. 3b). However, 5xFAD mice with ablated meningeal lymphatic vessels demonstrated marked deposition of amyloid-β in the meninges (Fig. 3b), as well as macrophage recruitment to large amyloid-β aggregates (Fig. 3c). Photoacoustic imaging one week after lymphatic ablation showed that there were no differences in blood flow and oxygenation between 5xFAD mice from the different groups (Extended Data Fig. 9a–c). Analysis of lymphoid and myeloid cell populations in the meninges (Extended Data Fig. 9d) demonstrated a significant increase in the number of macrophages upon lymphatic ablation compared to both control groups (Extended Data Fig. 9e), which might be correlated with increased amyloid-β deposition and inflammation in the meninges. Notably, along with meningeal amyloid-β pathology, we observed an aggravation of brain amyloid-β burden in the hippocampi of 5xFAD mice with dysfunctional meningeal lymphatic vessels (Fig. 3d–g). A similar outcome was observed in J20 transgenic mice after a total of three months of meningeal lymphatic ablation (Extended Data Fig. 9f); amyloid-β aggregates had formed in the meninges (Extended Data Fig. 9g) and the amyloid-β plaque load in the hippocampi of these mice was significantly increased (Extended Data Fig. 9h–k).

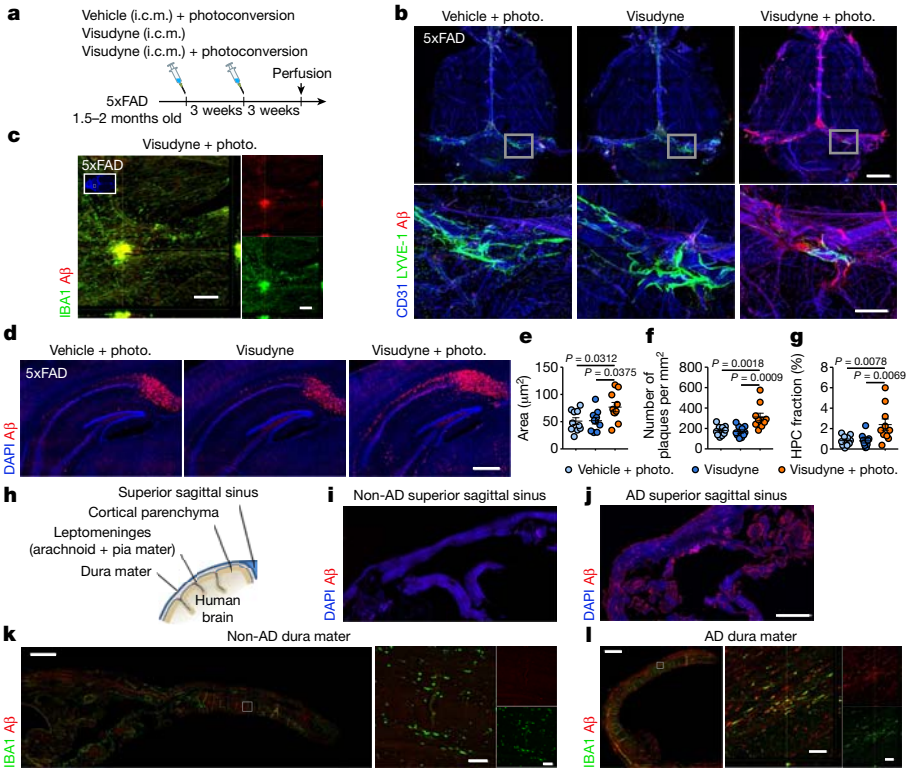

Fig. 3 | Ablation of meningeal lymphatic vessels aggravates amyloid-β pathology in transgenic mice with Alzheimer's disease. a, Young–adult 5xFAD mice were subjected to meningeal lymphatic ablation or control procedures. Procedures were repeated three weeks later and amyloid-β (Aβ) pathology was assessed six weeks after the initial intervention. **b**, Staining for CD31, LYVE-1 and amyloid-β in meninges. Scale bars, 2 mm and 500 μm (inset). **c**, Orthogonal view of IBA$^+$ macrophages clustering around an amyloid-β plaque in meninges of a 5xFAD mouse with ablated lymphatic vessels. Scale bars, 200 μm. **d**, Representative images of DAPI and amyloid-β in the hippocampus of 5xFAD mice from each group. Scale bar, 500 μm. **e**–**g**, Quantification of amyloid-β plaque size (**e**), number (**f**) and coverage (**g**) in the hippocampus of 5xFAD mice. Data in **e**–**g** are mean ± s.e.m., $n = 10$ per group, one-way ANOVA with Bonferroni's post hoc test. **a**–**g**, Data are representative of two independent experiments. **h**, Staining for amyloid-β pathology was performed in sections of brains with attached leptomeninges (Extended Data Fig. 9) and of meningeal dura mater from patients with Alzheimer's disease and controls. **i**, **j**, Meningeal superior sagittal sinus tissue of a control without Alzheimer's disease (non-AD) (**i**) and a patient with Alzheimer's disease (AD) (**j**) stained with DAPI and for amyloid-β. Scale bar, 2 mm. **k**, **l**, Meningeal dura mater tissue of a control without Alzheimer's disease (**k**) and a patient with Alzheimer's disease (**l**) stained for IBA1 and amyloid-β. Scale bars, 1 mm and 50 μm (orthogonal view inset). Data in **h**–**l** are from $n = 8$ controls and $n = 9$ patients with Alzheimer's disease and are representative of two independent experiments.

The observed meningeal amyloid-β pathology in mice after ablation of the meningeal lymphatic vessels led us to assess meningeal amyloid-β pathology in patients with Alzheimer's disease (Fig. 3h). Staining for amyloid-β in the brains of nine patients with Alzheimer's disease and eight controls without Alzheimer's disease (Extended Data Table 1) revealed, as expected, marked parenchymal deposition of amyloid-β in the brains of patients with Alzheimer's disease, but not in the brains of the controls without Alzheimer's disease (Extended Data Fig. 9l, m). Notably, when compared to tissue from controls, all samples from patients with Alzheimer's disease demonstrated striking vascular amyloid-β pathology in the cortical leptomeninges (Extended Data Fig. 9l, m) and amyloid-β deposition in the dura mater adjacent to the superior sagittal sinus (Fig. 3i, j) or further away from the sinus (Fig. 3k, l). Macrophages in the dura of cases with Alzheimer's disease were also found in close proximity to amyloid-β deposits (Fig. 3l). These findings showed that prominent meningeal amyloid-β deposition observed in patients with Alzheimer's disease is also observed in mouse models of Alzheimer's disease after meningeal lymphatic vessel ablation.

Discussion

Taken together, the present findings highlight the importance of meningeal lymphatic drainage in brain physiology. Meningeal lymphatic dysfunction in young–adult mice results in impaired brain perfusion by CSF and in learning and memory deficits. Aged mice demonstrated significant disruption of meningeal lymphatic function, which may underlie some of the aspects of age-associated cognitive decline. Augmentation of meningeal lymphatic drainage in aged mice can ultimately facilitate the clearance of CSF and ISF macromolecules from the brain, resulting in improved cognitive function. We also show that transgenic mouse models of Alzheimer's disease recapitulate many features of brain amyloid-β pathology observed in patients with Alzheimer's disease, but not the deposition of amyloid-β observed in the dura mater. However, inducing meningeal lymphatic dysfunction in mouse models of Alzheimer's disease worsened amyloid-β pathology in the meninges and in the brain. It would be interesting to see whether transgenic mice with Alzheimer's disease, particularly the ones with a less aggressive phenotype, when sufficiently aged, would exhibit meningeal amyloid-β pathology. Furthermore, taking into account the role of the brain vascular endothelium and of other components of the blood–brain barrier, such as pericytes, in the excretion of amyloid-β from the brain[7–9,42], it would be very interesting to explore a possible connection between age-associated meningeal lymphatic dysfunction, impaired CSF and ISF recirculation, and decreased fitness of the blood–brain barrier and its cellular components.

Finally, it is vital to determine whether ageing-related changes in meningeal lymphatic drainage might affect the efficacy of current therapies for Alzheimer's disease, such as antibody-based treatments[43]. Modulation of meningeal lymphatic function in aged individuals might represent a novel preventive therapeutic strategy, not only to delay initiation and progression of Alzheimer's disease but also for use against other brain proteinopathies that are exacerbated by ageing.

Online content

Any Methods, including any statements of data availability and Nature Research reporting summaries, along with any additional references and Source Data files, are available in the online version of the paper at https://doi.org/10.1038/s41586-018-0368-8.

Received: 29 September 2017; Accepted: 15 June 2018;
Published online 25 July 2018.

1. Hašek, M., Chutna, J., Sládecek, M. & Lodin, Z. Immunological tolerance and tumor allografts in the brain. *Nature* **268**, 68–69 (1977).
2. Louveau, A., Harris, T. H. & Kipnis, J. Revisiting the mechanisms of CNS immune privilege. *Trends Immunol*. **36**, 569–577 (2015).
3. Kipnis, J. Multifaceted interactions between adaptive immunity and the central nervous system. *Science* **353**, 766–771 (2016).
4. Louveau, A. et al. Structural and functional features of central nervous system lymphatic vessels. *Nature* **523**, 337–341 (2015).
5. Aspelund, A. et al. A dural lymphatic vascular system that drains brain interstitial fluid and macromolecules. *J. Exp. Med*. **212**, 991–999 (2015).
6. Absinta, M. et al. Human and nonhuman primate meninges harbor lymphatic vessels that can be visualized noninvasively by MRI. *eLife* **6**, e29738 (2017).
7. Deane, R. et al. apoE isoform-specific disruption of amyloid β peptide clearance from mouse brain. *J. Clin. Invest*. **118**, 4002–4013 (2008).
8. Zhao, Z. et al. Central role for PICALM in amyloid-β blood–brain barrier transcytosis and clearance. *Nat. Neurosci*. **18**, 978–987 (2015).
9. Deane, R. et al. RAGE mediates amyloid-β peptide transport across the blood–brain barrier and accumulation in brain. *Nat. Med*. **9**, 907–913 (2003).
10. Mildner, A. et al. Distinct and non-redundant roles of microglia and myeloid subsets in mouse models of Alzheimer's disease. *J. Neurosci*. **31**, 11159–11171 (2011).
11. Keren-Shaul, H. et al. A unique microglia type associated with restricting development of Alzheimer's disease. *Cell* **169**, 1276–1290 (2017).
12. Iliff, J. J. et al. A paravascular pathway facilitates CSF flow through the brain parenchyma and the clearance of interstitial solutes, including amyloid β. *Sci. Transl. Med*. **4**, 147ra111 (2012).
13. Kress, B. T. et al. Impairment of paravascular clearance pathways in the aging brain. *Ann. Neurol*. **76**, 845–861 (2014).
14. Peng, W. et al. Suppression of glymphatic fluid transport in a mouse model of Alzheimer's disease. *Neurobiol. Dis*. **93**, 215–225 (2016).
15. Brookmeyer, R., Abdalla, N., Kawas, C. H. & Corrada, M. M. Forecasting the prevalence of preclinical and clinical Alzheimer's disease in the United States. *Alzheimers Dement*. **14**, 121–129 (2018).
16. Erkkinen, M. G., Kim, M. O. & Geschwind, M. D. Clinical neurology and epidemiology of the major neurodegenerative diseases. *Cold Spring Harb. Perspect. Biol*. **10**, a033118 (2018).
17. Benilova, I., Karran, E. & De Strooper, B. The toxic Aβ oligomer and Alzheimer's disease: an emperor in need of clothes. *Nat. Neurosci*. **15**, 349–357 (2012).
18. Joachim, C. L., Duffy, L. K., Morris, J. H. & Selkoe, D. J. Protein chemical and immunocytochemical studies of meningovascular β-amyloid protein in Alzheimer's disease and normal aging. *Brain Res*. **474**, 100–111 (1988).
19. Xu, Z. et al. Deletion of aquaporin-4 in APP/PS1 mice exacerbates brain Aβ accumulation and memory deficits. *Mol. Neurodegener*. **10**, 58 (2015).
20. Chevalier, S., Ferland, G. & Tuchweber, B. Lymphatic absorption of retinol in young, mature, and old rats: influence of dietary restriction. *FASEB J*. **10**, 1085–1090 (1996).
21. Hos, D., Bachmann, B., Bock, F., Onderka, J. & Cursiefen, C. Age-related changes in murine limbal lymphatic vessels and corneal lymphangiogenesis. *Exp. Eye Res*. **87**, 427–432 (2008).
22. Nagai, T., Bridenbaugh, E. A. & Gashev, A. A. Aging-associated alterations in contractility of rat mesenteric lymphatic vessels. *Microcirculation* **18**, 463–473 (2011).
23. Tammela, T. et al. Photodynamic ablation of lymphatic vessels and intralymphatic cancer cells prevents metastasis. *Sci. Transl. Med*. **3**, 69ra11 (2011).
24. Kilarski, W. W. et al. Optimization and regeneration kinetics of lymphatic-specific photodynamic therapy in the mouse dermis. *Angiogenesis* **17**, 347–357 (2014).
25. Escobedo, N. et al. Restoration of lymphatic function rescues obesity in Prox1-haploinsufficient mice. *JCI Insight* **1**, e85096 (2016).
26. Ringstad, G., Vatnehol, S. A. S. & Eide, P. K. Glymphatic MRI in idiopathic normal pressure hydrocephalus. *Brain* **140**, 2691–2705 (2017).
27. Zeppenfeld, D. M. et al. Association of perivascular localization of aquaporin-4 with cognition and Alzheimer disease in aging brains. *JAMA Neurol*. **74**, 91–99 (2017).
28. Rudy, J. W., Huff, N. C. & Matus-Amat, P. Understanding contextual fear conditioning: insights from a two-process model. *Neurosci. Biobehav. Rev*. **28**, 675–685 (2004).
29. Owen, S. F. et al. Oxytocin enhances hippocampal spike transmission by modulating fast-spiking interneurons. *Nature* **500**, 458–462 (2013).
30. Zhang, G. et al. Hypothalamic programming of systemic ageing involving IKK-β, NF-κB and GnRH. *Nature* **497**, 211–216 (2013).
31. Liebl, J. et al. Cdk5 controls lymphatic vessel development and function by phosphorylation of Foxc2. *Nat. Commun*. **6**, 7274 (2015).
32. Jeltsch, M. et al. CCBE1 enhances lymphangiogenesis via A disintegrin and metalloprotease with thrombospondin motifs-3-mediated vascular endothelial growth factor-C activation. *Circulation* **129**, 1962–1971 (2014).
33. Shin, J. W. et al. Prox1 promotes lineage-specific expression of fibroblast growth factor (FGF) receptor-3 in lymphatic endothelium: a role for FGF signaling in lymphangiogenesis. *Mol. Biol. Cell* **17**, 576–584 (2006).
34. Saaristo, A. et al. Lymphangiogenic gene therapy with minimal blood vascular side effects. *J. Exp. Med*. **196**, 719–730 (2002).
35. Karkkainen, M. J. et al. A model for gene therapy of human hereditary lymphedema. *Proc. Natl Acad. Sci. USA* **98**, 12677–12682 (2001).
36. Joukov, V. et al. A recombinant mutant vascular endothelial growth factor-C that has lost vascular endothelial growth factor receptor-2 binding, activation, and vascular permeability activities. *J. Biol. Chem*. **273**, 6599–6602 (1998).
37. Han, J. et al. Vascular endothelial growth factor receptor 3 controls neural stem cell activation in mice and humans. *Cell Rep*. **10**, 1158–1172 (2015).
38. Meshi, D. et al. Hippocampal neurogenesis is not required for behavioral effects of environmental enrichment. *Nat. Neurosci*. **9**, 729–731 (2006).
39. Harris, J. A. et al. Many neuronal and behavioral impairments in transgenic mouse models of Alzheimer's disease are independent of caspase cleavage of the amyloid precursor protein. *J. Neurosci*. **30**, 372–381 (2010).
40. Palop, J. J. et al. Aberrant excitatory neuronal activity and compensatory remodeling of inhibitory hippocampal circuits in mouse models of Alzheimer's disease. *Neuron* **55**, 697–711 (2007).
41. Oakley, H. et al. Intraneuronal β-amyloid aggregates, neurodegeneration, and neuron loss in transgenic mice with five familial Alzheimer's disease mutations: potential factors in amyloid plaque formation. *J. Neurosci*. **26**, 10129–10140 (2006).
42. Sagare, A. P. et al. Pericyte loss influences Alzheimer-like neurodegeneration in mice. *Nat. Commun*. **4**, 2932 (2013).
43. Sevigny, J. et al. Addendum: The antibody aducanumab reduces Aβ plaques in Alzheimer's disease. *Nature* **546**, 564 (2017).

Acknowledgements We thank S. Smith for editing the manuscript, J. Roy for MRI expertise, N. Al Hamadani for animal care, G. Oliver (Feinberg School of Medicine, Northwestern University, Chicago) for *Prox1*$^{+/-}$ mice. This work was supported by grants from the National Institutes of Health/National Institute on Aging (AG034113 and AG057496), the Cure Alzheimer's Fund, Owens Family Foundation and the Thomas H. Lowder Family Foundation (awarded to J.K.), the Hobby Foundation (awarded to A.V. and S.T.A.) and American Cancer Society (IRG 81-001-26 awarded to J.M.M.). We thank all members of the Kipnis Laboratory and the BIG center for their valuable comments during numerous discussions of this work.

Reviewer information *Nature* thanks D. Holtzman and the other anonymous reviewer(s) for their contribution to the peer review of this work.

Author contributions S.D.M. designed and performed the experiments, analysed and interpreted the data and wrote the manuscript; A.L. designed and performed the experiments and participated in manuscript preparation; A.V. developed the software (Lymph4D) for MRI data processing and analysis; I.S. performed surgeries and behavioural testing; C.C. performed T2-weighted MRI, magnetic resonance angiography (MRA) and magnetic resonance venography (MRV) acquisition and data analysis; R.C.C. made hydrogels for transcranial peptide delivery; K.M.K. carried out brain T1-weighted MRI acquisition; S.O.-G. and E.F. carried out RNA-seq experiments; D.R., K.E.V., R.D.P., W.B., N.D. and R.B. assisted with experimental procedures; R.C. and S.H. carried out photoacoustic imaging; S.S.R. and J.M.M. provided resources and were involved in experimental design; M.B.L. provided human tissue samples; C.C.O. helped with RNA-seq raw data analysis, data interpretation and manuscript writing; S.T.A. participated in the development of the software (Lymph4D), provided resources and intellectual contributions; J.K. designed the experiments, provided intellectual contributions, oversaw data analysis and interpretation and wrote the manuscript.

Competing interests J.K. is an Advisor to PureTech Health/Ariya.

Additional information
Extended data is available for this paper at https://doi.org/10.1038/s41586-018-0368-8.
Supplementary information is available for this paper at https://doi.org/10.1038/s41586-018-0368-8.
Reprints and permissions information is available at http://www.nature.com/reprints.
Correspondence and requests for materials should be addressed to S.D.M. and J.K.
Publisher's note: Springer Nature remains neutral with regard to jurisdictional claims in published maps and institutional affiliations.

METHODS

Mouse strains and housing. Male or female wild-type mice (C57BL/6J background) were bred in-house, purchased from the Jackson Laboratory or provided by the National Institutes of Health/National Institute on Ageing. All mice were maintained in the animal facility for habituation for at least one week before the start of the manipulation/experimentation. C57BL/6J wild-type mice were tested at 2–3, 12–14 and 20–24 months of age. Male hemizygous B6.Cg-Tg(*PDGFB-APPSwInd*)20Lms/2Mmjax (J20, JAX 006293) and B6.Cg-Tg(*APPSwFlLon,PSEN1*M146L*L286V*)6799Vas/Mmjax (5xFAD, JAX 008730) were purchased from the Jackson Laboratory and bred in-house on a C57BL/6J background. J20 hemizygous mice present diffuse amyloid-β deposition in the dentate gyrus and neocortex at 5-7 months, with all transgenic mice exhibiting plaques by the age of 8–10 months[44]. 5xFAD hemizygous mice overexpress the transgene constructs under neural-specific elements of the mouse thymocyte differentiation antigen 1 promoter and have accelerated accumulation of 42-residue amyloid-β peptides (amyloid-β_{42}) and deposition of amyloid and gliosis in the brain starting at two months of age, with marked amyloid plaque load without major behavioural deficits at five months[45]. In-house bred male transgene carriers and non-carrier (wild-type) littermates were used at different ages that are indicated throughout the manuscript. *Prox1*^{LacZ} mice (designated *Prox1*$^{+/-}$ mice in this manuscript) on a NMRI background (provided by G. Oliver, Northwestern University, Chicago) were also bred in-house and used in this study as a constitutive model for dysfunctional lymphatic vessels[46]. Mice of all strains were housed in an environment with controlled temperature and humidity, on 12 h light:dark cycles (lights on at 7:00), and fed with regular rodent's chow and sterilized tap water ad libitum. All experiments were approved by the Institutional Animal Care and Use Committee of the University of Virginia.

Intra-cisterna magna injections. Mice were anaesthetized by intraperitoneal (i.p.) injection of a mixed solution of ketamine (100 mg kg^{-1}) and xylazine (10 mg kg^{-1}) in saline. The skin of the neck was shaved and cleaned with iodine and 70% ethanol, ophthalmic solution placed on the eyes to prevent drying and the head of the mouse was secured in a stereotaxic frame. After making a skin incision, the muscle layers were retracted and the cisterna magna exposed. Using a Hamilton syringe (coupled to a 33-gauge needle), the volume of the desired tracer solution was injected into the CSF-filled cisterna magna compartment. For brain CSF influx and lymphatic drainage experiments, 2 or 5 μl of Alexa Fluor 594- or 647-conjugated OVA (Thermo Fisher Scientific), at 0.5 mg ml^{-1} in artificial CSF (597316, Harvard Apparatus UK), were injected at a rate of 2.5 μl min^{-1}. After injecting, the syringe was left in place for additional 2 min to prevent backflow of CSF. The neck skin was then sutured, after which the mice were subcutaneously injected with ketoprofen (2 mg kg^{-1}) and allowed to recover on a heat pad until fully awake. For details regarding changes in intracranial pressure associated with this injection methodology see 'Intracranial pressure measurements' and Extended Data Fig. 2.

Intracranial pressure measurements. Mice were anaesthetized by i.p. injection with ketamine and xylazine in saline and the skin was incised to expose the skull. A 0.5-mm diameter hole was drilled in the skull above the right parietal lobe. Using a stereotaxic frame, a pressure sensor catheter (model SPR100, Millar) was inserted perpendicularly into the cortex at a depth of 1 mm. To record changes in intracranial pressure (ICP), the pressure sensor was connected to the PCU-2000 pressure control unit (Millar). For measurements of ICP while performing i.c.m. injections of 2 or 5 μl of tracer (following the same i.c.m. injection procedure as describe above), after stabilization of the signal (around a minute after insertion of the probe), average pressure was calculated over 1 min right before start injecting (pre-injection), over the last min of injection (during injection), over the last min of extra time used to prevent CSF backflow (post-injection with syringe in) and over the last 2 min of recording, specifically between minute 4 and 6 after taking out the syringe (post-injection with syringe out). For measurements in non-injected mice or in mice at different time-points (30, 60 and 120 min post-injection) after i.c.m. injection of 2, 5 or 10 μl of tracer, ICP was recorded for 6 min after stabilization of the signal and the average pressure was calculated over the last 2 min of recording (between minute 4 and 6 of the recording). All animals were euthanized at the conclusion of the measurement.

Meningeal lymphatic vessel ablation. Selective ablation of the meningeal lymphatic vessels was achieved by i.c.m. injection and transcranial photoconversion of visudyne (verteporfin for injection, Valeant Ophtalmics). visudyne was reconstituted following the manufacturer's instructions and 5 μl was injected i.c.m. following the procedure described in 'Intra-cisterna magna injections'. After 15 min, an incision was performed in the skin to expose the skull bone and visudyne was photoconverted by pointing a 689-nm-wavelength non-thermal red light (Coherent Opal Photoactivator, Lumenis) to five different spots above the intact skull (1 on the injection site, 1 on the superior sagittal sinus, 1 at the junction of all sinuses and 2 on the transverse sinuses). Each spot was irradiated with a light dose of 50 J per cm^2 at an intensity of 600 mW per cm^2 for a total of 83 s. Controls were injected with the same volume of visudyne (without the photoconversion step) or sterile saline plus photoconversion (vehicle/photoconversion). The scalp skin was then sutured, after which the mice were subcutaneously injected with ketoprofen (2 mg kg^{-1}) and allowed to recover on a heat pad until fully awake.

Lymphatic vessel ligation. Surgical ligation of the lymphatics afferent to the dCLNs was performed as described previously[47]. In brief, mice were anaesthetized by i.p. injection with ketamine and xylazine in saline, the skin of the neck was shaved and cleaned with iodine and 70% ethanol and ophthalmic solution placed on the eyes to prevent drying. A midline incision was made 5 mm superior to the clavicle. The sternocleidomastoid muscles were retracted and the dCLNs were exposed on each side. Ligation of the afferent lymphatic vessels on each side was performed with 10-0 synthetic, non-absorbable sutures. Control mice were subjected to a sham surgery consisting of the skin incision and retraction of the sternocleidomastoid muscle only. The skin was then sutured, after which the mice were subcutaneously injected with ketoprofen (2 mg kg^{-1}) and allowed to recover on a heat pad until fully awake.

Brain parenchymal injections. Mice were anaesthetized by i.p. injection of ketamine and xylazine in saline and the head was secured in a stereotaxic frame. An incision was made in the skin to expose the skull and a hole was drilled at 1.5 mm in the anterior–posterior axis and −1.5 mm in the medial–lateral axis relative to bregma. Then, using a Hamilton syringe (coupled to a 33-gauge needle) placed at 2.5 mm in the dorsal–ventral axis (relative to bregma), 1 μl of Alexa Fluor 647-conjugated OVA (at 0.5 mg ml^{-1}), HiLyte Fluor 647-conjugated amyloid-β_{42} (at 0.05 μg ml^{-1}, AnaSpec, Inc.) or BODIPY FL-conjugated low-density lipoprotein (LDL) from human plasma (at 0.1 mg ml^{-1}, Thermo Fisher Scientific) in artificial CSF were injected at a rate of 0.2 μl min^{-1} into the brain parenchyma. Concentrations of the injected fluorescent amyloid-β_{42} and LDL molecular tracers were chosen in order to be comparable to levels detected in the brain ISF of transgenic mice with Alzheimer's disease[47] and in plasma of C57BL/6 mice[48], respectively. After injecting, the syringe was left in place for additional 5 min to prevent backflow. The scalp skin was then sutured, after which the mice were subcutaneously injected with ketoprofen (2 mg kg^{-1}) and allowed to recover on a heat pad until further experiments.

AAV delivery. For experiments in which the effect of viral-mediated expression of mVEGF-C (NM_009506.2) on meningeal lymphatic vessels was assessed, 2 μl of artificial CSF containing 10^{13} genome copies per ml of AAV1-CMV-mVEGF-C, or control AAV1-CMV-eGFP (AAV1, adeno-associated virus serotype 1; CMV, cytomegalovirus promoter; eGFP, enhanced green fluorescent protein; purchased from Vector BioLabs, Philadelphia), were injected directly into the cisterna magna CSF at a rate of 2 μl min^{-1}, following the procedure described in 'Intra-cisterna magna injections'.

Transcranial recombinant VEGF-C delivery. A hydrogel of 1.4% hyaluronic acid and 3% methylcellulose alone (vehicle) or with 200 ng ml^{-1} of encapsulated human VEGF-C (PeproTech) or VEGF-C156S (R&D Systems) was prepared as described elsewhere[49]. In brief, lyophilized, sterile methylcellulose (4000 cP, Sigma-Aldrich) and sterile hyaluronic acid (1,500–1,800 kDa, Sigma-Aldrich) were sequentially dissolved in sterile 0.1 M phosphate buffered saline (PBS) at 4 °C overnight. Lyophilized VEGF-C or VEGF-C156S were resuspended as particulate at 2,000 ng ml^{-1} in 0.5% sterile methylcellulose in PBS. The particulate solution, or vehicle (0.5% methylcellulose), was mixed into the hydrogel pre-solution at 1:10, and loaded into a syringe for gelation at 37 °C. The methylcellulose provided more stability, by promoting thermal gelation, and increased the hydrophobic properties of the gel[49], sustaining the release of VEGF-C or VEGF-C156S up to 7–10 days in vitro (verified using an ELISA for human VEGF-C, R&D Systems). The hydrogels were prepared on the day of the experiment and kept warm inside the individual syringes until applied onto the skull of the mouse. The mouse was anaesthetized by i.p. injection of ketamine and xylazine in saline and the head was secured in a stereotaxic frame. An incision was made in the scalp skin and the skull was thinned at the junction of all sinuses and above the transverse sinus. The shear-thinning properties of the polymers allowed the extrusion of 100 μl of each hydrogel solution from the syringe into the thinned skull surface. The scalp skin was then sutured on top of the solidified hydrogel, after which the mice were subcutaneously injected with ketoprofen (2 mg kg^{-1}) and allowed to recover on a heat pad until fully awake. Taking the release kinetics of 7−10 days into account, hydrogels were reapplied, following the same methodology, two weeks after the first treatment.

MRI acquisitions and analysis. All MRI acquisitions were performed at the University of Virginia Molecular Imaging Core facilities in a 7T Clinscan system (Bruker) equipped with a 30-mm diameter cylindrical RF Coil. Detailed descriptions of MRI data acquisition, processing and analysis (including mathematical models and equations) can be found in the Supplementary information.

Photoacoustic imaging. Adult mice were maintained under anaesthesia with 1.5% isoflurane and at a constant body temperature with the aid of a heat pad. A surgical incision was made in the scalp and the fascia was removed to expose the skull. One day before the imaging, the skull over the region of interest was thinned to the desired thickness (~100 μm). Mice were then imaged by multi-parametric

photoacoustic microscopy, which is capable of simultaneously imaging oxygen saturation of hemoglobin (sO_2) and blood flow speed as described previously[50]. Using the oxy-haemoglobin and deoxy-haemoglobin values, recorded using two nanosecond-pulsed lasers (532 and 559 nm), it is possible to compute the final sO_2. Correlation analysis of adjacent A-line signals allows the quantification of blood flow speed within individual vessels. By segmenting major vessels within the region of interest, average values of the blood flow speed and sO_2 were extracted for quantitative analysis.

Open field test. The open field test was performed following a published protocol[51] with minor modifications. Mice were carried to the behaviour room to habituate at least 30 min before starting the test. Mice were then placed into the open field arena (made of opaque white plastic material, 35 cm × 35 cm) by a blinded experimenter and allowed to explore the arena for 15 min. Total distance (cm) and percentage of time spent in the centre (22 cm × 22 cm) were quantified using video tracking software (TopScan, CleverSys, Inc.).

NLR test. The novel location recognition test was performed following a published protocol[52] with modifications. The experimental apparatus used in this study was the same square box made of opaque white plastic (35 cm × 35 cm) used in the open field test. The mice were first habituated to the apparatus for 15 min. Two different plastic objects (one red and the other blue, and with different shapes) were then positioned in the arena, in two corners next to each other and 5 cm away from each adjacent arena wall. Mice were then placed in the arena (by a blinded experimenter), facing the wall furthest away from the objects and allowed to explore the arena and objects for 10 min. After 24 h, the mice were placed in the same box with the same two objects, but one of them had switched location and was placed in a new quadrant, obliquely to the familiar object (novel location test). The time spent exploring the objects in the familiar and novel locations was also measured for 10 min. Exploration of an object was assumed when the mouse approached an object and touched it with its vibrissae, snout or forepaws and was measured using a video tracking software (TopScan, CleverSys, Inc.). The object location preference (percentage of time with object) was calculated as the exploration time of the objects in the familiar or in the novel location/total exploration time.

CFC test. This behavioural test was performed following a published protocol[53] with modifications. In this associative learning task, mice were presented with a neutral conditioned cue stimulus that is paired with an aversive unconditioned stimulus in a particular context. The mice learned that the chamber context and the cue stimulus predicted the aversive stimulus and this elicited a specific behavioural response, namely freezing. Mice were brought into the testing room to acclimatize for at least 30 min before testing. For the test, we used two Habitest chambers (Coulbourn Instruments) with stainless grid floors attached to a shock generator for foot shock delivery and dimly illuminated with a white-fluorescent light bulb. The chambers were cleaned and made odour-free before starting the experiment and between each session (or each mouse). The fear conditioning test was conducted over two days. On day 1, mice were placed in the conditioning chamber and allowed to habituate for 3 min. Then, mice received three pairs of cue-aversive stimuli, consisting of tone (18 s, 5 kHz, 75 dB)–shock (2 s, 0.5 mA) pairings, separated by an interval of 40 s (total of 3 min). Mice were returned to their home cage 30 s after the last shock presentation. On day 2, mice were tested and scored for conditioned fear to the training context for 3 min (context test), but with no presentation of the cue stimulus. After 2 h, mice were presented to a novel context, in which the light intensity was slightly increased, the grid and walls of the chamber were covered by plastic inserts with different texture and colours and the inside of the chamber was scented with a paper towel dabbed with vanilla extract placed under the floor grid. In this last session, mice were placed in the conditioning chamber and allowed to habituate for 3 min, after which they received a continuous cue stimulus (tone) for an additional 3 min (cued test). Mice behaviour was recorded by a digital video camera mounted above the conditioning chamber and freezing was manually scored by a blinded experimenter using the Etholog v.2.2 software. Parameters analysed included the percentage of time freezing during the 3 min of the context test and the last 3 min of the cued test.

MWM test. The MWM test was performed as described previously[53], but with modifications. Mice were transported to the behaviour room to habituate at least 30 min before starting the test. The MWM test consisted of four days of acquisition, one day of probe trial and two days of reversal. In the acquisition, mice performed four trials per day, for four consecutive days, to find a hidden 10-cm diameter platform located 1 cm below the water surface in a pool that was 1 m in diameter. Tap water was made opaque with nontoxic tempera white paint and the water temperature was kept at 23 ± 1 °C. A dim light source was placed within the testing room and only distal visual cues were available above each quadrant of the swimming pool to aid in the spatial navigation and location of the submerged platform. The latency to platform, that is, the time required by the mouse to find and climb onto the platform, was recorded for up to 60 s. Each mouse was allowed to remain on the platform for 20 s and was then moved from the maze to its home cage. If the mouse did not find the platform within 60 s, it was manually placed on the platform and returned to its home cage after 20 s. The inter-trial interval for each mouse was at least 5 min. On day 5, the platform was removed from the pool, and each mouse was tested in a probe trial for 60 s. On days 1 and 2 of the reversal, without changing the position of the visual cues, the platform was placed in the quadrant opposite to the original acquisition quadrant and the mouse was retrained for four trials per day. All MWM testing was performed between 13:00 and 18:00, during the lights-on phase, by a blinded experimenter. During the acquisition, probe and reversal, data were recorded using the EthoVision automated tracking system (Noldus Information Technology). The mean latency (in seconds) of the four trials was calculated for each day of test trials. The percentage of time in the platform quadrant was calculated for the probe trial. Additionally, using a modified version of previous published methods[54,55], the full tracked path taken by each mouse in every trial of the acquisition and reversal days was used to classify the type of navigation strategy as either egocentric or allocentric by a blinded experimenter. The mean percentage of allocentric navigation of four trials was calculated for each day.

CSF and tissue collection and processing. Mice were given a lethal dose of anaesthetics by i.p. injection of euthasol (10% v/v in saline). When needed, CSF was collected from the cisterna magna using a 0.5-mm diameter borosilicate glass pipette with internal filament and immediately stored at −80 °C. Mice were then transcardially perfused with ice-cold PBS with heparin (10 U ml^{-1}). Deep cervical lymph nodes were dissected and drop-fixed in 4% paraformaldehyde (PFA) for 12 h at 4 °C. After stripping the skin and muscle from the bone, the head was collected and drop-fixed in 4% PFA. After removal of the mandibles and the skull rostral to maxillae, the top of the skull (skullcap) was removed with surgical curved scissors by cutting clockwise, beginning and ending inferior to the right post-tympanic hook and kept in PBS and 0.02% azide at 4 °C until further use. The brains were kept in 4% PFA for an additional 24 h (48 h in total). Fixed brain and dCLNs were then washed with PBS, cryoprotected with 30% sucrose and frozen in Tissue-Plus OCT compound (Thermo Fisher Scientific). Fixed and frozen brains were sliced (100-μm thick sections) with a cryostat (Leica) and kept in PBS and 0.02% azide at 4 °C. Frozen lymph nodes were sliced (30-μm thick sections) in a cryostat, collected onto gelatin-coated Superfrost Plus slides (Thermo Fisher Scientific) and stored at −20 °C. Alternatively, after euthanizing and perfusing the mouse, the skullcap was removed from the head of the mouse and drop-fixed in 4% PFA for 12 h, and the brains were immediately collected into OCT compound, snap-frozen in dry ice and stored at −80 °C. Fresh-frozen brains were then sliced (30-μm thick sections) in the cryostat and sections were directly collected onto Superfrost Plus slides and kept at −20 °C until further use. Fixed meninges (dura mater and arachnoid) were carefully dissected from the skullcaps with Dumont #5 forceps (Fine Science Tools) and kept in PBS and 0.02% azide at 4 °C until further use.

Amyloid-β measurement in CSF. To measure the concentration of amyloid-β peptides (ranging in size from amyloid-β_{37} to amyloid-β_{42}) in the CSF of J20 mice, an in-house direct ELISA assay was used. In brief, Nunc MaxiSorp flat-bottom 96-well plates (ThermoFisher Scientific) were coated with 2 μl of CSF diluted in 98 μl of a KH_2PO_4/K_2HPO_4 buffer (pH 8.0) solution (1:50 dilution factor), for 2 h at 37 °C. After washing with PBS and 0.05% Tween-20 (Sigma-Aldrich), a blocking step with PBS and 1% skim milk was performed for 1 h at room temperature. Then, consecutive incubations for 1 h at room temperature were performed: first, with rabbit anti-amyloid-β_{37-42} (Cell Signaling, clone D54D2, 1:500); second, with biotinylated goat anti-rabbit (Vector Laboratories, BA-1000, 1:500); and third, with streptavidin–horseradish peroxidase (1:2,500, Sigma-Aldrich). Each incubation step was separated by two washes with PBS containing 0.05% Tween 20 and followed by another two washes with PBS alone. Finally, a citrate-phosphate buffer (pH 4.3) solution containing 0.1% of 2,2′-azino-bis(3-ethylbenzothiazoline-6-sulfonic acid) diammonium salt (ABTS, Sigma-Aldrich) was added to each well and absorbance was read at 405 nm. The standard curve used to extrapolate the concentration of amyloid-β in the CSF was obtained using known concentrations of human amyloid-β_{42} (AnaSpec, Inc.) that ranged from 0.1 to 100 ng ml^{-1} (considering the linearity of the assay). Data processing was done with Excel and statistical analysis was performed using Prism 7.0a (GraphPad Software).

Human samples. Autopsy specimens of human brain and dura from patients without ($n = 8$) or with ($n = 9$) Alzheimer's disease were obtained from the Department of Pathology at the University of Virginia (UVA). All samples were from consenting patients that gave no restriction to the use of their body for research and teaching (through an UVA's Institutional Review Board for Health Sciences Research). Diagnosis criteria and pathological score were performed following the National Institute on Ageing–Alzheimer's Association guidelines[56], based on the ABC (Amyloid, Braak, CERAD) score, for seven of the cases with Alzheimer's disease; old guidelines were used to diagnose and score two of the cases with Alzheimer's disease (Extended Data Table 1). All obtained samples were fixed in a 20% formalin solution and kept in paraffin blocks until further sectioning. Prior to immunohistochemical staining, slides containing 10-μm thick sections were heated to 70 °C for 30 min and deparaffinized by washing sections with xylene, 1:1 xylene:100%

ethanol (v/v), and 100, 95, 70 and 50% ethanol in water. Finally, tissue sections were rehydrated by rinsing with cold tap water.

Immunohistochemistry, imaging and quantifications. Mouse fresh-frozen brain sections were fixed with 4% PFA for 30 min, rinsed in dH_2O and subjected to a heat-induced antigen retrieval step with 10 mM citrate buffer for 20 min. After deparaffinization, sections of human brain or dura were subjected to the same antigen retrieval step for 20 min. The steps described next were applied for mouse fresh-frozen and fixed free-floating brain sections, lymph node sections on slide, meningeal whole-mounts and human fixed tissue. For immunofluorescence staining, tissue was rinsed in PBS and washed with PBS and 0.5% Triton X-100 for 10 min, followed by incubation in PBS and 0.5% Triton X-100 containing 0.5% of normal serum (either goat or chicken) and 0.5% bovine serum albumin (BSA) for 1 h at room temperature. This blocking step was followed by incubation with appropriate dilutions of primary antibodies: anti-LYVE-1–eFluor 660 or anti-LYVE-1–Alexa Fluor 488 (eBioscience, clone ALY7, 1:200), anti-CD31 (Millipore Sigma, MAB1398Z, clone 2H8, 1:200), anti-IBA1 (Abcam, ab5076, 1:300), anti-GFAP (Millipore Sigma, ab5541, 1:300), anti-AQP4 (Millipore Sigma, A5971, 1:200), anti-Ki-67 (Abcam, ab15580, 1:100), anti-human amyloid-β_{16} (BioLegend, clone 6E10, 1:200), anti-amyloid-β_{37-42} (Cell Signaling, clone D54D2, 1:300) and anti-GFP (Abcam, ab6556, 1:300) in PBS and 0.5% Triton X-100 containing 0.5% of normal serum and 0.5% BSA overnight at 4 °C. Meningeal whole-mounts or tissue sections were then washed three times for 5 min at room temperature in PBS and 0.5% Triton X-100 followed by incubation with the appropriate chicken, goat or donkey Alexa Fluor 488, 546, 594 or 647 anti-rat, -goat, -rabbit, -mouse or -Armenian hamster IgG antibodies (Thermo Fisher Scientific, 1:500) for 1 or 2 h at room temperature in PBS and 0.5% Triton X-100. After incubating for 10 min with 1:2,000 DAPI in PBS, the tissue was washed three times for 5 min with PBS at room temperature and mounted with Aqua-Mount (Lerner) and glass coverslips. Preparations were stored at 4 °C for no more than one week until images were acquired either using a wide-field microscope (Leica) or a confocal microscope (FV1200 Laser Scanning Confocal Microscope, Olympus). Quantitative analysis using the acquired images was performed using Fiji software. For the assessment of brain fluorescent tracer influx or efflux or AQP4 coverage, 10 representative brain sections were imaged using the wide-field microscope and the mean area fraction was calculated using Microsoft Excel. For lymph nodes, the area fraction of drained fluorescent tracer or lymphatic vessels was assessed in alternate sections (representing a total of 10–15 sections per sample) using a confocal microscope and the mean was calculated for each sample. Area of coverage by $CD31^+$ blood vessels and $AQP4^+$ astrocyte endfeet in the brain cortex was achieved by calculating the mean value of 10 representative fields (5 images in each cerebral hemisphere) per sample that was acquired using a confocal microscope. For lymphatic vessel diameter, images of the same region of the superior sagittal sinus or of the transverse sinus were acquired using a confocal microscope and the mean of 100 individual lymphatic vessel diameter measurements (50 measurements in each lymphatic vessel lining the sinus using Fiji) was calculated for each sample by a blinded experimenter (due to different criteria used by distinct experimenters, this quantification method is often associated with a variability of ±15% in absolute diameter values). For assessment of meningeal lymphatic vessel coverage and complexity, images of meningeal whole-mounts were acquired using a confocal microscope and Fiji was used for quantifications. When applicable, the same images were used to assess the percentage of field coverage by $LYVE\text{-}1^-CD31^+$ vessels. To quantify the number of proliferating $Ki\text{-}67^+$ cells in the hippocampal dentate gyrus, images of the entire dentate gyrus of three representative brain sections per sample were obtained using a confocal microscope. Fiji was used to assess the number of $Ki\text{-}67^+$ cells per mm^2 of DAPI cells that composed the granular zone, which were then used to calculate the average density of cells per sample. For assessment of amyloid burden in the dorsal hippocampus, tile scans of the entire dorsal hippocampus from 10 coronal brain sections (~180 μm apart from each other) were obtained using a confocal microscope. Fiji was used to quantify amyloid plaque size, number and total coverage.

Flow cytometry. Mice were injected i.p. with euthasol solution and were then transcardially perfused with ice-cold PBS with heparin. Individual meninges were immediately dissected from the skullcap of the mouse and digested for 15 min at 37 °C with 1.4 U ml^{-1} of collagenase VIII (Sigma Aldrich) and 35 U ml^{-1} of DNase I (Sigma Aldrich) in complete media consisting of DMEM (Gibco) with 2% FBS (Atlas Biologicals), 1% L-glutamine (Gibco), 1% penicillin–streptomycin (Gibco), 1% sodium pyruvate (Gibco), 1% non-essential amino-acids (Gibco) and 1.5% HEPES (Gibco). The cell pellets were washed, resuspended in ice-cold fluorescence-activated cell sorting (FACS) buffer (pH 7.4; 0.1 M PBS; 1 mM EDTA and 1% BSA) and stained for extracellular markers with the following antibodies: rat anti-CD90.2–FITC (553013; BD Biosciences), rat anti-CD11b–FITC (557396; BD Biosciences), rat monoclonal anti-CD19–PE (12-0193-82; eBioscience), rat anti-CD45–PerCP–Cy5.5 (550994; BD Biosciences), rat anti-Ly6C–PerCP–Cy5.5 (560525; BD Biosciences), mouse anti-NK1.1–PE–Cy7 (552878; BD Biosciences), rat anti-Ly6G–PE–Cy7 (560601; BD Biosciences), rat anti-CD4–APC (553051; BD Biosciences), rat anti-CD45–Alexa Fluor 700 (560510; BD Biosciences), hamster anti-TCRb–BV711 (563135; BD Biosciences), rat anti-CD8–Pacific blue (558106; BD Biosciences) and rat anti-Siglec-F–BV421 (562681; BD Biosciences). Cell viability was determined by using the Zombie Aqua Fixable Viability Kit following the manufacturer's instructions (BioLegend). After an incubation period of 30 min at 4 °C, cells were washed and fixed in 1% PFA in PBS. Fluorescence data were collected with a Gallios Flow Cytometer (Beckman Coulter, Inc.) then analysed using FlowJo software (Tree Star, Inc.). In brief, singlets were gated using the height, area and the pulse width of the forward and side scatter and then viable cells were selected as $AQUA^-$. Cells were then gated for the appropriate cell-type markers. An aliquot of unstained cells of each sample was counted using Cellometer Auto2000 (Nexcelor) to provide accurate counts for each population. Data processing was done with Excel and statistical analysis was performed using Prism 7.0a (GraphPad Software, Inc.).

Sorting of meningeal LECs. To obtain a suspension of meningeal LECs from the meninges of young–adult (2–3 months) and old (20–24 months) mice using FACS, mice were euthanized by i.p. injection of euthasol and transcardially perfused with ice-cold PBS with heparin. Skullcaps were quickly collected and meninges (dura mater and arachnoid) were dissected using Dumont #5 forceps in complete medium composed of DMEM (Gibco) with 2% FBS (Atlas Biologicals), 1% L-glutamine (Gibco), 1% penicillin–streptomycin (Gibco), 1% sodium pyruvate (Gibco), 1% non-essential amino-acids (Gibco) and 1.5% HEPES (Gibco). Individual meninges were then incubated with 1 ml of complete medium with 1.4 U ml^{-1} of collagenase VIII (Sigma-Aldrich) and 35 U ml^{-1} of DNase I (Sigma-Aldrich) for 15 min at 37 °C. Individual samples consisted of cell suspensions pooled from 10 meninges that were obtained after filtration through a 70-μm nylon-mesh cell strainer. Cell suspensions were then pelleted, resuspended in ice-cold FACS buffer containing DAPI (1:1,000, Thermo Fisher Scientific), anti-CD45–BB515 (1:200, clone 30-F11, BD Biosciencess), anti-CD31–Alexa Fluor 647 (1:200, clone 390, BD Biosciencess) and anti-podoplanin–PE (1:200, clone 8.1.1, eBioscience) and incubated for 15 min at 4 °C. Cells were then washed and resuspended in ice-cold FACS buffer. In brief, singlets were gated using the pulse width of the side scatter and forward scatter. Cells negative for DAPI were selected as viable cells. The LECs were then gated as $CD45^-CD31^+$podoplanin$^+$ (see Extended Data Fig. 6 for representative dot plots) and sorted into a 96-well plate containing 100 μl of lysis buffer (Arcturus PicoPure RNA Isolation Kit, Thermo Fisher Scientific) using the Influx Cell Sorter (BD Biosciencess) that is available at the University of Virginia Flow Cytometry Core Facility.

RNA extraction and sequencing. For total RNA extraction from the whole hippocampus, the tissue was macrodissected from the brain in ice-cold PBS, immersed in the appropriate volume of extraction buffer from the RNA isolation kit, immediately snap-frozen in dry ice and stored at −80 °C until further use. After defrosting on ice, samples were mechanically dissociated in extraction buffer and RNA was isolated using the kit components according to the manufacturer's instructions (RNeasy mini kit, 74106, QIAGEN). The Illumina TruSeq Stranded Total RNA Library Prep Kit was used for cDNA library preparation from total RNA samples. Sample quality control was performed using an Agilent 4200 TapeStation Instrument, using the Agilent D1000 kit, and using the Qubit Fluorometer (Thermo Fisher Scientific). For RNA-seq, libraries were loaded on to a NextSeq 500 (Illumina) using an Illumina NextSeq High Output (150 cycle) cartridge (FC-404-2002).

Total RNA was extracted from LECs (previously sorted by FACS) using the Arcturus PicoPure RNA Isolation Kit (Thermo Fisher Scientific), following the manufacturer's instructions. All RNA sample processing (including linear RNA amplification and cDNA library generation) and RNA-seq was performed by HudsonAlpha Genomic Services Laboratory.

The raw sequencing reads (FASTQ files) were first chastity filtered, which removes any clusters that have a higher than expected intensity of the called base compared to other bases. The quality of the reads was then evaluated using FastQC[57], and after passing quality control, the expression of the transcripts was quantified against the UCSC mm10 genome[58] using Salmon[59]. These transcript abundances were then imported into R and summarized with tximport[60], and then DESeq2[61] was used to normalize the raw counts, perform exploratory analysis (for example, principal component analysis), and to perform differential expression analysis. Before differential expression analysis of the meningeal LECs from the adult versus old mice dataset, surrogate variable analysis[62] (SVA) was used to identify and adjust for latent sources of unwanted variation as implemented in the SVA package[63]. The *P* values from the differential expression analysis were corrected for multiple hypothesis testing with the Benjamini–Hochberg false-discovery rate procedure (adjusted *P* value). Functional enrichment of differential expressed genes, using gene sets from Gene Ontology (GO) and Kyoto Encyclopedia of Genes and Genomes (KEGG), was determined with Fisher's exact test as implemented in the

clusterProfiler[64] Bioconductor package. Heat maps of the differential expressed genes and enriched gene sets were generated with the R package pheatmap[65]. Normalized counts of selected transcripts were used to calculate the fold change relative to respective controls.

Statistical analysis and reproducibility. Sample sizes were chosen on the basis of standard power calculations (with $\alpha = 0.05$ and power of 0.8) performed for similar experiments that were previously published[51–53]. In general, statistical methods were not used to re-calculate or predetermine sample sizes. The Kolmogorov–Smirnov test was used to assess normal distribution of the data. Variance was similar within comparable experimental groups. Animals from different cages, but within the same experimental group, were selected to assure randomization. Experimenters were blinded to the identity of experimental groups from the time of euthanasia until the end of data collection and analysis for at least one of the independent experiments. Statistical tests for each figure were justified to be appropriate. One-way ANOVA, with Bonferroni's post hoc test or Holm-Sidak's post hoc test, was used to compare three independent groups. Two-group comparisons were made using two-tailed unpaired Mann–Whitney *U*-tests. For comparisons of multiple factors (for example, age versus treatment), two-way ANOVA with Bonferroni's post hoc test was used. Repeated-measures two-way ANOVA with Bonferroni's post hoc test was used for day versus treatment comparisons with repeated observations. Statistical analysis (data are always presented as mean ± s.e.m.) was performed using Prism 7.0a (GraphPad Software, Inc.).

Reporting summary. Further information on experimental design is available in the Nature Research Reporting Summary linked to this paper.

Code availability. Lymph4D software code is available online under GNU General Public license v.3.0 at https://github.com/avaccari/Lymph4D. Custom code used during the current study are also available from the corresponding authors upon reasonable request.

Data availability. Source Data for quantifications mentioned either in the text or shown in graphs plotted in Figs. 1–3 and Extended Data Figs. 1–9 are available in the online version of the paper. RNA-seq datasets have been deposited online in the Gene Expression Omnibus (GEO) under accession numbers GSE104181, GSE104182 and GSE113351. The datasets generated and/or analysed during the current study are also available from the corresponding authors upon reasonable request.

44. Mucke, L. et al. High-level neuronal expression of $A\beta_{1-42}$ in wild-type human amyloid protein precursor transgenic mice: synaptotoxicity without plaque formation. *J. Neurosci.* **20**, 4050–4058 (2000).
45. Richard, B. C. et al. Gene dosage dependent aggravation of the neurological phenotype in the 5XFAD mouse model of Alzheimer's disease. *J. Alzheimers Dis.* **45**, 1223–1236 (2015).
46. Harvey, N. L. et al. Lymphatic vascular defects promoted by *Prox1* haploinsufficiency cause adult-onset obesity. *Nat. Genet.* **37**, 1072–1081 (2005).
47. Cirrito, J. R. et al. In vivo assessment of brain interstitial fluid with microdialysis reveals plaque-associated changes in amyloid-β metabolism and half-life. *J. Neurosci.* **23**, 8844–8853 (2003).
48. Hinder, L. M., Vincent, A. M., Hayes, J. M., McLean, L. L. & Feldman, E. L. Apolipoprotein E knockout as the basis for mouse models of dyslipidemia-induced neuropathy. *Exp. Neurol.* **239**, 102–110 (2013).
49. Caicco, M. J. et al. A hydrogel composite system for sustained epi-cortical delivery of cyclosporin A to the brain for treatment of stroke. *J. Control. Release* **166**, 197–202 (2013).
50. Ning, B. et al. Ultrasound-aided multi-parametric photoacoustic microscopy of the mouse brain. *Sci. Rep.* **5**, 18775 (2015).
51. Derecki, N. C. et al. Wild-type microglia arrest pathology in a mouse model of Rett syndrome. *Nature* **484**, 105–109 (2012).
52. Louveau, A. et al. Impaired spatial memory in mice lacking CD3ζ is associated with altered NMDA and AMPA receptors signaling independent of T-cell deficiency. *J. Neurosci.* **33**, 18672–18685 (2013).
53. Derecki, N. C. et al. Regulation of learning and memory by meningeal immunity: a key role for IL-4. *J. Exp. Med.* **207**, 1067–1080 (2010).
54. Janus, C. Search strategies used by APP transgenic mice during navigation in the Morris water maze. *Learn. Mem.* **11**, 337–346 (2004).
55. Garthe, A. & Kempermann, G. An old test for new neurons: refining the Morris water maze to study the functional relevance of adult hippocampal neurogenesis. *Front. Neurosci.* **7**, 63 (2013).
56. Montine, T. J. et al. National Institute on Aging–Alzheimer's Association guidelines for the neuropathologic assessment of Alzheimer's disease: a practical approach. *Acta Neuropathol.* **123**, 1–11 (2012).
57. Andrews, S. *FastQC: a Quality Control Tool for High Throughput Sequence Data*. Babraham Bioinformatics version 0.11.7. https://www.bioinformatics.babraham.ac.uk/projects/fastqc/ (2010).
58. Harrow, J. et al. GENCODE: the reference human genome annotation for The ENCODE Project. *Genome Res.* **22**, 1760–1774 (2012).
59. Patro, R., Duggal, G., Love, M. I., Irizarry, R. A. & Kingsford, C. Salmon provides fast and bias-aware quantification of transcript expression. *Nat. Methods* **14**, 417–419 (2017).
60. Soneson, C., Love, M. I. & Robinson, M. D. Differential analyses for RNA-seq: transcript-level estimates improve gene-level inferences. *F1000Res.* **4**, 1521 (2015).
61. Love, M. I., Huber, W. & Anders, S. Moderated estimation of fold change and dispersion for RNA-seq data with DESeq2. *Genome Biol.* **15**, 550 (2014).
62. Leek, J. T. & Storey, J. D. Capturing heterogeneity in gene expression studies by surrogate variable analysis. *PLoS Genet.* **3**, e161 (2007).
63. Leek, J. T., Johnson, W. E., Parker, H. S., Jaffe, A. E. & Storey, J. D. The sva package for removing batch effects and other unwanted variation in high-throughput experiments. *Bioinformatics* **28**, 882–883 (2012).
64. Yu, G., Wang, L. G., Han, Y. & He, Q. Y. clusterProfiler: an R package for comparing biological themes among gene clusters. *OMICS* **16**, 284–287 (2012).
65. Kolde, R. *Pretty Heatmaps*. R package version 1.0.8 https://github.com/raivokolde/pheatmap (2015).